Vertically Layered Multi-Pair Interdigital Electrodes within a Single Sheet of Paper for High Energy Density

Yeon Woo Kim,[a] In Hyeok Oh,[a] and Suk Tai Chang*[a]

A paper-based supercapacitor (SC) is a promising flexible energy storage device for wearable electronics. Paper is an alternative flexible substrate to conventional substrates such as metal foil or plastics. Paper's porous structure can be applied as a large surface area of electrode to store more charge. Paper can also be used as a separator between each electrode. We propose a simple method for vertically integrating a multi-pair of interdigital electrodes within only a single sheet of paper.

The integrated multi-electrodes were fully separated because of a removable wax barrier. The integrated multi-pair interdigital electrodes in a paper were used as ultra-thin SCs combined in parallel. With an inner space of paper, the device volume can be reduced with high energy density while preserving flexibility. The energy density was 86.58 $\mu Wh\,cm^{-2}$, which is three orders of magnitude higher energy density than a single SC at the same size.

Introduction

In the last decade, flexible supercapacitors (SCs) have attracted significant research attention in the field of energy storage devices for flexible and wearable electronics.[1–5] Comparatively to conventional capacitors and batteries, SCs have higher energy and power densities, respectively.[4] Moreover, SCs have other advantages, such as an extremely long lifetime and rapid charge and discharge times.[5] However, their low energy densities are a severe limitation for alternative energy storage devices compared with batteries.

Various active materials, substrates, and electrode architectures have been researched using a large surface area capable of storing more charges to improve the low energy densities.[6–10] Paper is a suitable alternative flexible substrate to conventional substrates, such as metal foil or plastics, with disadvantages such as weak adhesion and large mass densities.[11] Paper-based electrodes exhibit high electrochemical performance because paper's high porosity provides ample space for more active material deposition while preserving flexibility.[12–17] Nevertheless, a combination of multi-unit SCs has been applied for high electrochemical performance.[18–21] This combination of SCs increases the device's total volume as much as when combined. Therefore, much effort has been required to produce high energy density while decreasing device volume.

We propose a simple method for integrating a multi-pair of interdigital electrodes in a single sheet of paper while maintaining device volume. Based on the above-described advantages of paper, a multi-pair of interdigital electrodes can be assembled vertically within only a single sheet of paper. In

this study, paper serves not only as a substrate but also as a separator. Therefore, the electrodes can be insulated by the cellulose network between each electrode. The energy storage performance can be maximized by using an inner space of the paper with no increment of device volume. To our knowledge, multi-layered electrode integration inside a single sheet of paper has not yet been performed.

We previously studied a wax pattern printing method for flexible metal electrodes on paper.[22] The wax is hydrophobic that it prevents the penetration of an aqueous solution and can be easily removed from the paper after the metal deposition. Moreover, the wax can be uniformly infiltrated within the paper through its pores, although the metal is already deposited inside the paper. Therefore, multi-electrodes can be assembled within a complex cellulose fiber network while maintaining the conductive disconnection of each electrode. In this study, a paper-based interdigital channel surrounded by hydrophobic wax as a capillary tube is fabricated in the middle of the paper.

This method uses a multi-pair of interdigital electrodes integrated vertically on the paper without changing the device volume. Citrate-capped gold nanoparticles (Au NPs) were used to form in-plane interdigital electrodes to demonstrate this concept. The Au NP solution infiltrated the paper-based interdigital channel by capillary action and deposited only on the cellulose fibers in the paper-based interdigital channel. Despite the pre-deposited interdigital electrode in the middle of the paper, other electrodes can be deposited on both sides of the paper surface using the wax printing method. We can achieve high SC energy density and maintain device volume using the proposed method because it also uses the space inside the paper. Moreover, the fabricated SC with a multi-pair of interdigital electrodes exhibits high stability. Linear resistances of the SC changed negligibly during the bending and folding test. The capacitance of the SC was changed negligibly during 6,000 cycles of the cyclic voltammetry (CV) curve.

[a] Y. W. Kim, I. H. Oh, Prof. S. T. Chang
School of Chemical Engineering and Materials Science
Chung-Ang University
84 Heukseok-ro, Dongjak-gu, Seoul 06974, Republic of Korea
E-mail: stchang@cau.ac.kr

Batteries & Supercaps

Research Article
doi.org/10.1002/batt.202200407

Chemistry Europe
European Chemical
Societies Publishing

Results and Discussion

The manufacturing process for the single-layered and three-layered interdigital Au-paper electrodes on a single sheet of paper is described in Figure 1 and the average size of the interdigital Au-paper electrode in Figure S1. In creating the interdigital paper channel in the middle of the paper, a wax interdigital pattern was first printed on both sides of the paper and heated. Subsequently, the Au NPs were penetrated and deposited on a cellulose fiber in the interdigital paper channel by the capillary action of the Au NPs solution. The carboxyl groups of the citrate ions that capped the Au NPs were strongly aligned to the hydroxyl groups of the cellulose fibers.[23] Because of the citrate ions' strong repulsive force, the Au NPs placed on the paper were not conductive because they were spread out. For the conductive Au electrode, Au ions were applied to the Au NPs to enhance Au size and reduce the spacing between Au particles. The interdigital Au-paper electrode can be produced in the middle of the paper using this technique.

Moreover, despite the pre-deposited single interdigital Au-paper electrode being in the middle of the paper, the interdigital Au-paper electrodes were deposited on both sides of the single interdigital Au-paper electrode using an additional wax pattern printing process—wax can easily penetrate the

paper regardless of whether it has the pre-deposited Au-paper electrode because of the paper's porosity. Our earlier study used wax printing and drop-casting techniques to deposit Au NPs on the paper surface.[22] However, it was challenging to deposit the Au NP layer in the middle of the paper using the drop-casting approach. Therefore, the capillary action method was applied for the middle Au NP layer of the paper in this study. Consequently, a vertically integrated multi-pair of the interdigital Au-paper electrodes could be produced on a single sheet of paper.

The printed wax vertical and lateral lengths, dependent on the heating time, are critical factors in manufacturing the vertically integrated multi-pair of interdigital electrodes on a single sheet of paper. The wax length changes (L) were caused by the molten wax permeation by capillary action as following the Lucas-Washburn equation:[24–27]

$$L = S \times t^{0.5}, \; S = ((D \times \gamma \times \cos\theta)/(4 \times \mu))^{0.5} \qquad (1)$$

where D, γ, μ, θ, and t are the pore size, surface tension, viscosity of the melting wax, contact angle, and heating time, respectively.

As depicted in Figure 2, the wax lengths correspond to the square root of the heating time according to the Lucas-Washburn equation. The wax vertical length change (L_z) is crucial for fabricating the middle Au NP layer on the paper and separating the three-layered Au-paper electrodes. The L_z is inversely proportional to the paper's middle Au NP layer thickness. By adjusting L_z, the middle Au NP layer can be controlled as thinly as possible for vertical separation of the three-layered electrodes. In this study, the L_z was measured with different heating times at 80 °C (Figure 2a). Before heating the printed wax on the paper, the wax thickness was an average of 78.5 μm. After heating for more than 40 s, although it was possible to measure the L_z, it was difficult for Au NPs solution to easily infiltrate to the designed length of the interdigital paper channel.

Based on these experiments, the heating time of the wax printed on both sides for fabricating the middle Au NP layer was fixed at 40 s. Consequently, 125 μm of the middle Au NP layer thickness was prepared within the paper. After Au enhancement of the middle Au NP layer, the top and bottom Au NP layers were fabricated on both sides of the middle Au-paper electrode. The wax lateral length change (L_{xy}) is critical in creating the top and bottom interdigital Au NP layers because the width between the anode and cathode finger electrode can be regulated as closely as possible for a high capacitance by modifying L_{xy}. The smallest wax width required to prevent the Au NPs solution from penetrating undesired space was 600 μm. The L_{xy} with different heating times at 100 °C was calculated as the average as follows:

$$L_{xy} = (W_f - W_i)/2 \qquad (2)$$

where W_f and W_i are the average wax width after and before heating, respectively (Figure 2b). L_{xy} was consistent with the
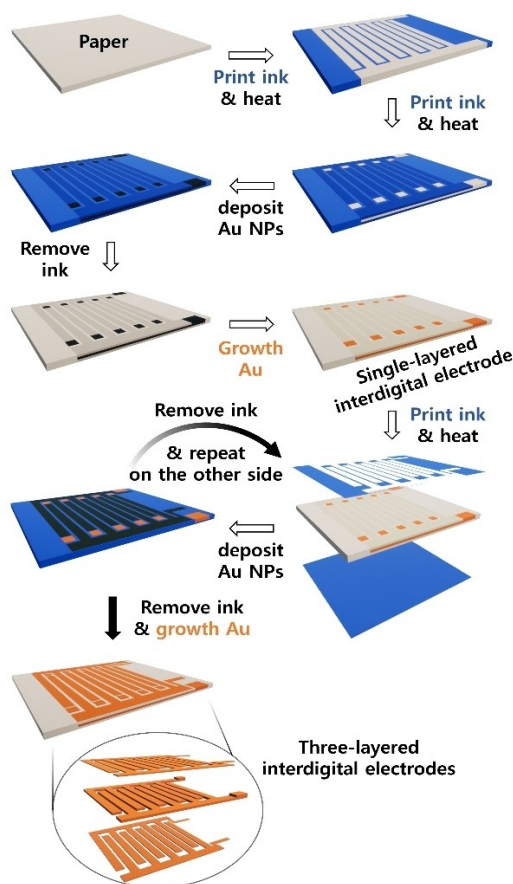

Figure 1. Schematics of fabricating three-layered interdigital Au-paper electrodes in a single sheet of paper.

Batteries & Supercaps

Research Article
doi.org/10.1002/batt.202200407

Chemistry Europe
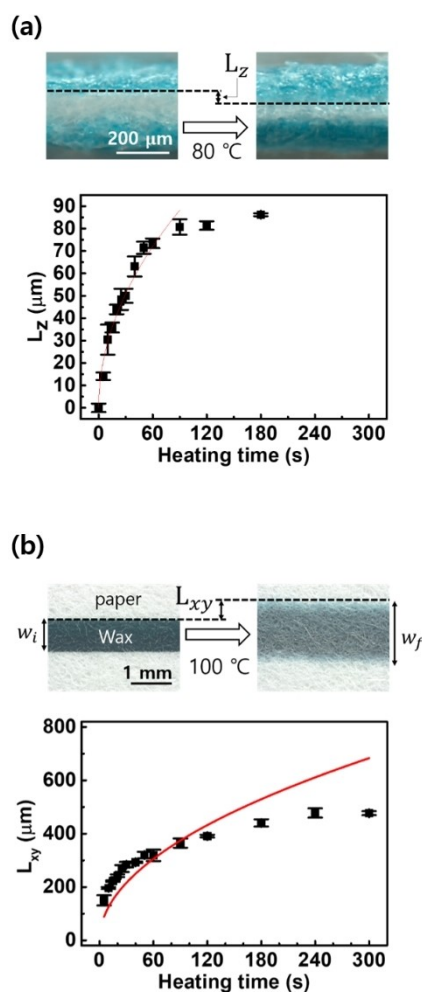European Chemical
Societies Publishing

Figure 2. Characterization of paraffin wax (solid ink) barrier. a) Cross-sectional images of a paper printed with cyan color wax on both sides before (left image) and after (right image) heating for 40 s at 80 °C and a plot of wax vertical length change (L_z) with respect to heating time. b) Top view images of a paper printed with cyan color wax before (left image) and after (right image) heating for 90 s at 100 °C and a plot of wax lateral length change (L_{xy}) with respect to heating time.

Figure 3. Characteristics of single interdigital Au-paper electrode on a sheet of paper. a) Schematic of single interdigital Au-paper electrode on a sheet of paper and cross-sectional FE-SEM image of a finger Au-paper. b) Energy-dispersive X-ray spectroscopy (EDS) images of single finger Au-paper. c) XPS analysis results of single Au-paper. Resistance profile with respect to d) bending radius, e) folding angle, and f) folding cycle of single Au-paper.

Lucas-Washburn equation only up to 90 s of the heating time because of the limited amount of the printed wax.

Based on these data, the heating time of the interdigital wax pattern for the top and bottom Au NP layer was fixed at 10 s. The heating time was appropriate for fabricating 826.6 μm of the thinnest width between finger electrodes while preventing unwanted penetration of the Au NPs solution. While using the fabricated interdigital Au NP layer for the conductive electrode, the amount of reducing agent (NH₂OH) of the Au enhance solution was characterized (Figure S2). Consequently, the linear resistance of the interdigital Au-paper electrode was minimized at an average of 9.88 Ω. The cross-sectional image of the fabricated single-layered interdigital Au-paper electrode is illustrated in Figure S3.

The characteristics of the single-layered interdigital Au-paper electrode are illustrated in Figure 3. The schematic and filed-emission scanning electron microscopy (FE-SEM) cross-sectional images are depicted in Figure 3(a). The single-layered
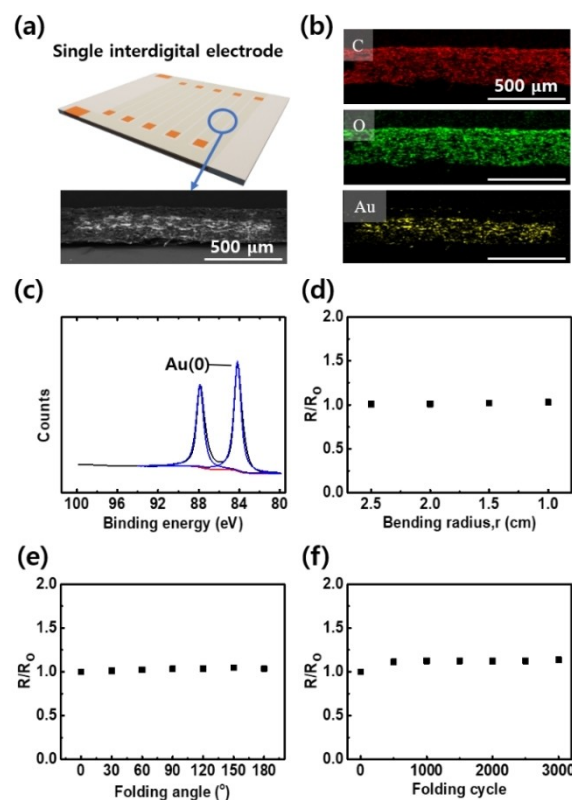
interdigital Au-paper electrode was manufactured completely in the middle of the paper. The presence of the Au-paper electrode was confirmed because Au ions were enhanced only on the Au NP layer in the middle of the paper (Figure 3b), and the porous network and large surface of the Au-paper electrode were observed (Figure S4). The Au 4f spectrum was obtained using X-ray photoelectron spectroscopy (XPS) to estimate the chemical composition. (Figure 3c). A doublet peak was observed at 84.18 and 87.88 eV, revealing the creation of a metallic Au(0).[28]

A stability test of the single-layered interdigital Au-paper electrode was achieved using the resistance profiles (Figure 3d–f). The bending stability of the single-layered interdigital Au-paper electrode was measured at a bending radius of 1.0–2.5 cm (Figure 3d). The linear resistance of the single-layered interdigital Au-paper electrode increased only 3% at 1 cm of the bending radius. The folding stability of the single-layered interdigital Au-paper electrode was confirmed with a folding angle of 30°–180° (Figure 3e). The linear resistance of the single-layered interdigital Au-paper electrode increased from 150° up to only 4.6%. Furthermore, only 13.6% of the linear resistance of the single-layered interdigital Au-paper electrode was observed during 3,000 folding cycles (Figure 3f). Therefore, the single-layered and three-layered interdigital Au-paper electrodes were verified.

Batteries & Supercaps

Research Article
doi.org/10.1002/batt.202200407

Chemistry
Europe

European Chemical
Societies Publishing

In applying the interdigital Au-paper electrode to the SC, MnO_2 was the active material in a pseudo-capacitive reaction. Anodic electrodeposition from a manganous acetate solution was used to deposit MnO_2 on the Au-paper. The cross-sectional FE-SEM image of the three-layered MnO_2–Au-paper finger electrode on a single sheet of paper is illustrated in Figure 4(a), and the EDS images are in Figure 4(b). The finger electrodes were fully separated within a single sheet of paper. Moreover, the porosity of the paper was preserved, and a sizeable electrochemical surface area of MnO_2 was observed, as illustrated in Figure S5.

X-ray diffraction (XRD) patterns were used to measure MnO_2–Au-paper crystallinity (Figure 4c). Five distinct peaks associated with pure crystalline gold were observed for the MnO_2–Au-paper electrode at $2\theta = 38.2°$, $44.4°$, $64.6°$, $77.5°$, and $81.7°$ compared with the bare paper.[29–32] Amorphous MnO_2

was deposited uniformly on the Au-paper based on the similar XRD patterns between the MnO_2–Au-paper and Au-paper electrodes. Furthermore, an XPS analysis of the MnO_2–Au-paper was performed to examine the components of the MnO_2–Au-paper. Three peaks at 530.03, 531.54, and 532.93 eV, associated with Mn–O–Mn, Mn–O–H, and H–O–H, were obtained by the deconvolution of the O1 spectra (Figure 4d). Based on the peaks of Mn–O–H and Mn–O–Mn bonds, MnO_2 deposition on the Au-paper electrode occurred. An H–O–H bond peak was caused by the MnO_2 prepared as $MnO_2 \cdot nH_2O$. As depicted in Figure 4(e), two distinct peaks in the Mn 2p spectra at 642.38 and 654.18 eV, which are the Mn 2p1/2 and Mn 2p 3/2 spin-orbit peaks of MnO_2, with a spin-energy separation of 11.8 eV, reveal the production of MnO_2.[33–39]

A single interdigital SC was measured in a PVA/Na_2SO_4 gel electrolyte in the potential range of 0–0.8 V to apply the single-layered interdigital MnO_2–Au-paper electrode as a symmetric SC. Cyclic voltammetry (CV) curves were measured at a scan rate of 20 mV s^{-1} for different masses of MnO_2 (Figure 5a). The CV curves have a suitable quasi-rectangular shape for an ideal capacitor. Galvanostatic charge and discharge (GCD) curves were measured at a current density of 0.5 mA cm^{-2} for different masses of MnO_2 (Figure 5b). The GCD curves have a typical triangular shape. From the GCD data, the areal capacitance was measured with respect to the current density for different MnO_2 masses (Figure 5c). The areal capacitance decreased with an increase in the current density. The highest areal capacitance was 0.42 F cm^{-2} at a MnO_2 mass loading of 4.0 mg cm^{-2} at 0.1 mA cm^{-2}.

The single-layered interdigital MnO_2–Au-paper electrode in the middle of the paper had high stability (Figure 5d). At a high scan rate, it demonstrated remarkable capacity retention of 98% for 6,000 cycles. Furthermore, the single SCs on the paper's surface exhibited high electrochemical performance for
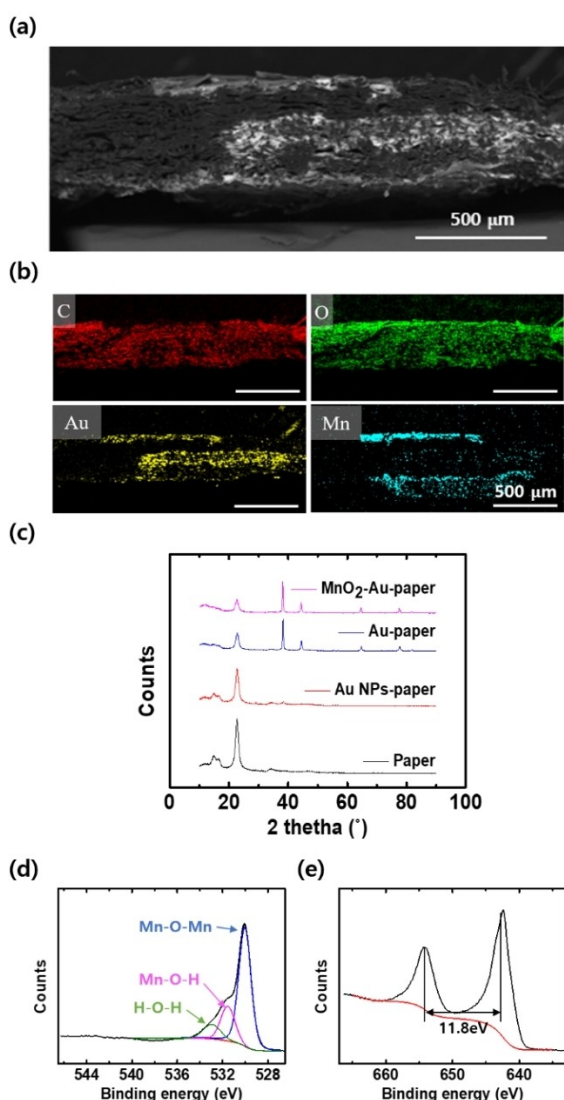

Figure 4. Characteristics of three-layered MnO_2–Au-paper electrode on single sheet of paper. a) Cross-sectional FE-SEM and b) EDS images of a finger electrode of three layered MnO_2–Au-paper. c) XRD patterns of paper, Au-NP paper, Au paper, and MnO_2–Au paper. d and e) XPS results for MnO_2–Au-paper.
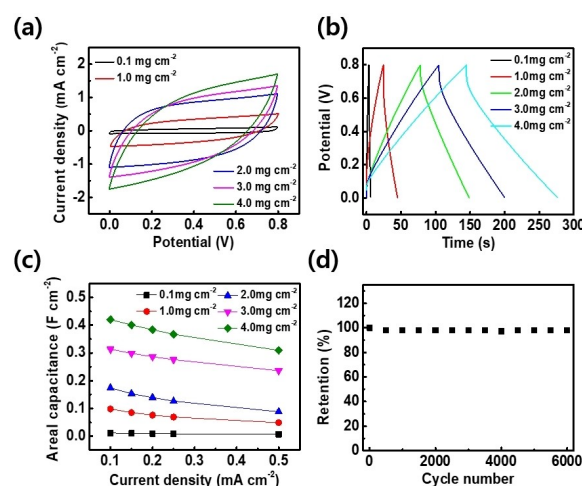

Figure 5. Electrochemical performance of single interdigital SC of MnO_2–Au-paper electrodes. a) CV curves at 20 mV s^{-1} and b) GCD curves at 0.5 mA cm^{-2} for different mass densities of MnO_2. c) Areal capacitance with respect to current density for different mass densities. d) Capacitance retention by cycle test of MnO_2–Au-paper electrode for 6,000 cycles at a scan rate of 500 mV s^{-1}.

a flexible paper-based SC, as depicted in Figure S6. Nyquist plots were investigated by electrochemical impedance spectroscopy (EIS) to confirm the influence of resistance on the electrode position. At the same MnO_2 mass loadings of 3.0 mg cm^{-2}, the equivalent series resistance (R_s) values of the single SC in the middle and the paper surface were 7.71 and 6.46 Ω. This R_s was low enough to verify that the electrons were transported quickly. Their EIS curves were nearly straight lines in the low-frequency range, indicating rapid ion diffusion in the electrode.[40,41] The single SC in the middle and the surface of the paper exhibited high capacity retention, as depicted in Figure S6(b), and excellent capacitance (Figure S6c and d). Hence, the interdigital MnO_2–Au-paper electrode exhibits excellent electrochemical performance regardless of the deposition position.

In this study, the interdigital MnO_2–Au-paper electrodes were integrated vertically as three-layered electrodes on only a single sheet of paper to achieve high energy density without changing the device volume. Compared with the single SC, the integrated three-layered interdigital electrode was prepared in a parallel circuit, as depicted in Figure 6(a). The amount of MnO_2 in the electrode was the same. The parallel SC had a conventional pseudo-rectangular shape of the CV curves without redox peaks and a typical triangular shape of GCD curves for different MnO_2 masses (Figure S7a and b). The areal capacitance was calculated with respect to the current density for different MnO_2 masses (Figure S7c). The CV curve of the parallel SC had a significantly larger area than that of the single SC (Figure 6b).

As depicted in Figure 6(c), the GCD curve of the parallel SC exhibited a conventional triangular shape with a small IR drop. The discharge time of the parallel SCs was three orders of magnitude longer than that of the single SC.[42] From the GCD data, the areal capacitance of the parallel SC was calculated with respect to the current density compared with the single

SC (Figure 6d). The maximum areal capacitance of the parallel SC was 0.34 F cm^{-2}, which was three orders of magnitude higher than that of the single SC, at a current density of 0.1 mA cm^{-2} for a MnO_2 mass loading of 1.0 mg cm^{-2}. Furthermore, the vertically integrated architecture of the parallel SC had high flexibility.

The capacitance retention of the parallel SC was investigated (Figure 7). As depicted in Figure 7(a and b), the capacitance retention was maintained at 84% of its initial value during the bending test up to a 1.0 cm bending radius and 85% of its initial value during the folding test with a folding angle of 180°. The capacitance retention of the parallel SC was preserved 86% of its initial value with a bending radius of 1.0 cm during 3000 bending cycles despite exposure to dry air (Figure 7c). On the other hand, the cyclic stability of the parallel SC was preserved at 92% for 6,000 cycles at a high current density in a closed space (Figure 7d). The capacitance retention of the device can be improved by applying a packaging process to prevent water evaporation from the PVA gel electrolyte. Hence, the vertically integrated interdigital electrode with MnO_2–Au-paper electrodes exhibited high flexibility and stability for application as a parallel flexible SC.

Energy and power densities are critical for determining an energy storage device's capability. The areal energy density (E_a) and power density (P_a) were measured from the areal capacitance (C_a) of the GCD data as follows:

$$E_a = (C_a \times V^2)/2 \tag{3}$$

$$P_a = E_a/\Delta t \tag{4}$$

where C_a, V and Δt are the areal capacitance, potential range and discharge time, respectively.

The area energy and power densities of our devices and the previous reported interdigital-electrode SCs are compared in
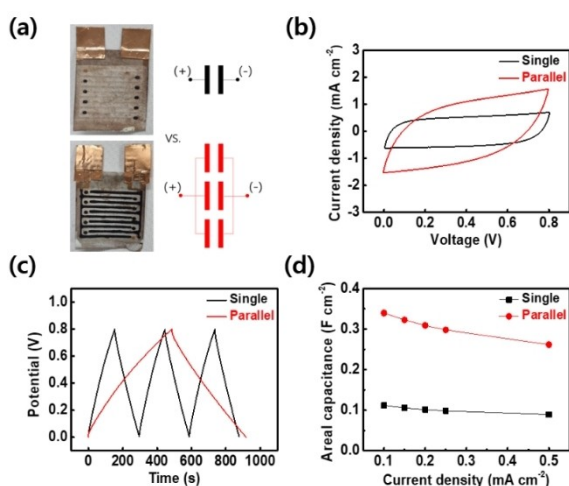

Figure 6. Electrochemical performance of interdigital SC of single and three-layered MnO_2–Au-paper electrodes. a) The single and three-layered interdigital MnO_2–Au-paper electrodes and each circuit diagram. b) CV curves at a scan rate of 20 mV s^{-1}, c) GCD curves at 0.15 mA cm^{-2}, and d) areal capacitance with respect to current density for single SC and parallel SC.
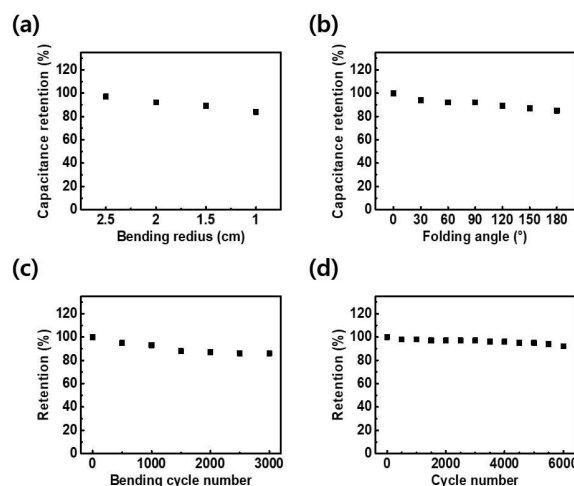
Figure 7. Electrochemical performance of parallel interdigital SC of three layer MnO_2–Au-paper electrodes. a) Bending radius and b) folding angle at a scan rate of 50 mV s^{-1} by CV. c) Bending stability for 3000 cycles at 1.0 cm of a bending radius. d) Cyclic stability of parallel SC at a scan rate of 500 mV s^{-1} by CV.

Batteries & Supercaps

Research Article
doi.org/10.1002/batt.202200407

Chemistry Europe
European Chemical
Societies Publishing

Figure 8. At the same current density of 0.1 mA cm^{-2}, P_a and E_a of the single SC were 0.16 and 27.87 µWh cm^{-2}. The single SC with the interdigital MnO$_2$–Au-paper electrode exhibited a higher energy density than previous reports of interdigital SCs.[36,42–51] For the parallel SC at the same current density of 0.1 mA cm^{-2}, the areal energy density was 86.58 µWh cm^{-2} at the same P_a of 0.16 mW cm^{-2}. The parallel SC had an E_a three orders of magnitude higher than the single SC. Consequently, the vertically integrated multi-pair of the interdigital MnO$_2$–Au-paper electrodes was fabricated using only a single sheet of paper without any device volume change in a parallel circuit for high energy density.

Conclusion

Multi-pair interdigital electrodes were integrated vertically within only a single sheet of paper for a flexible, high-energy SC while minimizing device volume. The simple wax printing method was used to prepare the paper SC. Despite the fibrous networks being randomly arranged on a single piece of paper, the interdigital electrodes were fabricated in the designed location by the hydrophobic wax pattern. After depositing active materials on metal-coated fibers of layered interdigital electrodes, a flexible single-layered paper SC demonstrated excellent stability and electrochemical performance while maintaining flexibility. The SC can be used in a parallel circuit for high energy density. The parallel SC exhibited a large areal capacitance of 0.974 F cm^{-2} at 0.1 mA cm^{-2} and maximum energy and power densities of 86.58 µWh cm^{-2} and 0.8 mW cm^{-2}. The excellent electrochemical performance of the fabricated paper SC suggests its use as a high-energy storage device using only one substrate to minimize device volume. Thus, our approach for fabricating paper-based SCs with multi-layered interdigital electrodes is promising for applications such as flexible energy storage devices and paper-based wearable electronics.
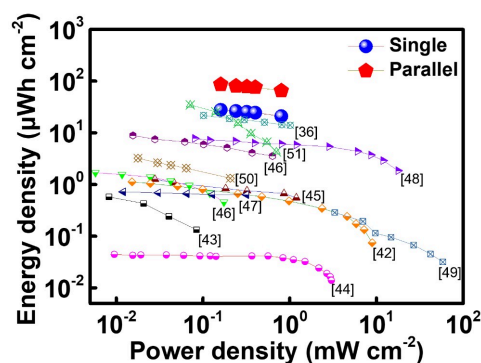

Figure 8. Ragone plot of single SC and parallel SC compared with previously reported interdigital-electrode SCs.

Experimental Section

Materials: Whatman grade 3 qualitative filter paper (390-µm thick, 6-µm porosity), gold(III) chloride solution (HAuCl$_4$), sodium citrate tribasic dehydrate, gold(III) chloride trihydrate (HAuCl$_4$·3H$_2$O), hydroxylamine hydrochloride (NH$_2$OH·HCl), manganese(II) acetate tetrahydrate, sodium sulfate (Na$_2$SO$_4$), and polyvinyl alcohol (PVA) were purchased from Sigma-Aldrich, USA. Toluene and isopropanol (IPA) were purchased from Daejung, Korea.

Synthesis of Au NP solution: For synthesizing the Au NP solution, 800 mL of deionized (DI) water was boiled at 100 °C with stirring at 400 rpm, and 277 µL HAuCl$_4$ was added to the boiled DI water. After the solution was mixed, 80 mL of 2.9 mM sodium citrate tribasic dehydrate was added. The yellow-colored solution turned transparent immediately. The solution color changed gradually from transparent to black, purple, and then red. The solution was then heated for 1 h with constant stirring to synthesize citrate-capped Au NPs and then cooled to room temperature (under 28 °C) with constant stirring. The solution's concentration was quantified by an ultraviolet (UV)-visible-near-infrared (NIR) spectrometer (V-670, Jasco, USA). The synthesized Au NP solution was highly concentrated by a stirring cell.

Fabrication of interdigital Au electrode inside middle of paper: An interdigital pattern of paraffin wax was printed on both sides of the filter paper using a Xerox ColorQube 8570 printer for the interdigital architecture. The patterned paper was heated to 100 °C for 5 min. Paraffin wax was re-printed on both sides of the interdigital area and then heated at 80 °C for 40 s to create the interdigital pattern inside the filter paper. Then, a pair of the interdigital electrode regions surrounded by the hydrophobic wax pattern was prepared inside the middle of the paper. The 0.8 wt% Au NP solution (400 µL) was penetrated on one side of the electrode region by capillary action. After drying at room temperature, the deposition process of Au NP solution was repeated on the opposite electrode region. The Au NP deposited paper (Au NP paper) was immersed in toluene at 94 °C for 1 hour to remove paraffin wax, was washed with pure toluene and IPA, and dried on a hotplate at 50 °C. The Au growth solution was prepared using 2.7 mM HAuCl$_4$·3H$_2$O (3 mL) and 254 mM NH$_2$OH·HCl (1 mL). The Au NP paper was immersed in the Au growth solution to induce a reaction on an orbital shaker (SK–O180-E, DLAB) at 200 rpm for 25 min. The Au growth process was repeated on the other side of the Au-grown paper. The resulting paper with the interdigital Au electrode (Au-paper) was washed with DI water and dried on the hotplate at 50 °C.

Fabrication of interdigital Au electrodes on Au-paper surface: Paraffin wax was printed on an entire area of one side of the Au-paper surface and heated for 5 min on the hotplate at 100 °C. The interdigital electrode pattern of paraffin wax was printed on the other side of the Au-paper surface and heated for 10 s on the hotplate at 100 °C. The 0.8 wt% Au NP solution (80 µL) was deposited on the interdigital electrode pattern and dried on the hotplate at 50 °C. After removing the paraffin wax by toluene and washing by pure toluene and IPA, this process was repeated on the other side to prepare the interdigital patterned Au NP deposited on both sides of the Au-paper surface. After Au NP deposition on both surfaces, the Au-paper was immersed in the Au growth solution prepared with 2.7 mM HAuCl$_4$·3H$_2$O (3 mL) and 12 mM NH$_2$OH·HCl solution (25 mL), and a reaction was induced on the orbital shaker at 200 rpm for 5 min. The Au-paper with the three-layered interdigital electrodes was washed with DI water and dried on the hotplate at 50 °C.

Fabrication of solid-state MnO$_2$–Au-paper SC: MnO$_2$ was deposited on the Au-paper electrode via anodic electrodeposition from a 1 M

manganous acetate solution at 1.3 V vs. Ag/AgCl to fabricate the solid-state SC of the interdigital Au-paper electrode. Moreover, the gel electrolyte solution was prepared using PVA and Na_2SO_4. The 10 wt% PVA solution (60 mL) and the 12 mM sodium sulfate solution (10 mL) were stirred at 120 °C until 10 mL of water evaporated. The gel electrolyte solution (PVA/Na_2SO_4) was then cooled to room temperature. The MnO_2—Au-paper was immersed in the PVA/Na_2SO_4 until the gel completely penetrated the paper and dried under ambient conditions for the solid-state MnO_2—Au-paper SC.

Characterization: Cross-sectional optical images of the paper were acquired using an Olympus BX-51 optical microscope equipped with a high-resolution ProRes CF Scan digital charge-coupled device camera (Jenoptik, Germany). Linear resistance was measured using a multimeter (34461A Keysight, USA) with a two-point probe system. Morphological images of the paper surfaces were acquired by field-emission scanning electron microscopy (FE-SEM) (Carl Zeiss, Germany). Cross-sectional FE-SEM images and energy-dispersive X-ray spectroscopy (EDS) results were acquired using a cooling cross-section polisher (IB-19520CCP, Japan) and FE-SEM (JSM-6700F, Japan). The crystal structure was examined using X-ray diffraction (XRD) (New D8-Advance, Bruker-AXS, Germany). Moreover, the device structures and chemical compositions were acquired using X-ray photoelectron spectroscopy (XPS) (K-alpha+, Thermo Fisher Scientific, USA).

Electrochemical measurements: CV, GCD, and EIS measurements of the MnO_2—Au-paper SC were obtained using a potentiostat (Electrochemical Workstation ZIVE SP1, WonATech, Korea). A three-electrode system was set up using a Pt coil electrode (counter electrode) and Ag/AgCl electrode (reference electrode) with a 1 M Na_2SO_4 liquid electrolyte. EIS was performed within a frequency range from 100 mHz to 100 kHz at a potential amplitude of 5 mV. The capacitance (C) of the MnO_2—Au-paper SC were calculated using Eqs. (1–4):

$$C = (I \times \Delta t)/\Delta V \text{ for GCD} \tag{5}$$

$$C_a = (4 \times C)/A \tag{6}$$

where I, Δt, ΔV, C_a, and A are the current, discharge time, potential window, areal capacitance, and area of the two electrodes and interspacing.

Acknowledgements

Conflict of Interest

The authors declare no conflict of interest.

Data Availability Statement

Data sharing is not applicable to this article as no new data were created or analyzed in this study.

[1] W. K. Chee, H. N. Lim, Z. Zainal, N. M. Huang, I. Harrison, Y. Andou, *J. Phys. Chem. C* **2016**, *120*, 4153–4172.

[2] N. Hillier, S. Yong, S. Beeby, *Energy Rep.* **2020**, *6*, 148–156.

[3] I. Shown, A. Ganguly, L.-C. Cheng, K-H. Chen, *Energy Sci. Eng.* **2015**, *3*, 2–26.

[4] L. Dong, C. Xu, Y. Li, Z.-H. Huang, F. Kang, Q.-H. Yang, X. Zhao, *J. Mater. Chem. A* **2016**, *4*, 4659–4685.

[5] X. Peng, L. Peng, C. Wu, Y. Xie, *Chem. Soc. Rev.* **2014**, *43*, 3303–3323.

[6] W. Raza, F. Ali, N. Raza, Y. Luo, K.-H. Kym, J. Yang, S. Kumar, A. Mehmood, E. E. Kwon, *Nano Energy* **2018**, *52*, 441–473.

[7] S. Najib, E. Erdem, *Nanoscale Adv.* **2019**, *1*, 2817–2827.

[8] L. Nyholm, G. Nyström, A. Mihranyan, M. Strømme, *Adv. Mater.* **2011**, *23*, 3751–3769.

[9] D. P. Dubal, J. G. Kim, Y. Kim, R. Holze, C. D. Lokhande, W. B. Kim, *Energy Technol.* **2014**, *2*, 325–341.

[10] Y. Da, J. Liu, L. Zhou, X. Zhu, X. Chen, L Fu, *Adv. Mater.* **2019**, *31*, 1802793.

[11] B. Yao, J. Zhang, T. Kou, Y. Song, T. Liu, Y. Li, *Adv. Sci.* **2017**, *4*, 1700107.

[12] Y. Lin, D. Gritsenko, Q. Liu, X. Lu, J. Xu, *ACS Appl. Mater. Interfaces* **2016**, *8*, 20501–20515.

[13] D. Zhao, Y. Zhu, W. Cheng, W. Chen, Y. Wu, H. Yu, *Adv. Mater.* **2021**, *33*, 2000619.

[14] K. Keum, J. W. Kim, S. Y. Hong, J. G. Son, S.-S. Lee, J. S. Ha, *Adv. Mater.* **2020**, *32*, 2002180.

[15] L. Hu, H. Wu, Y. Cui, *Appl. Phys. Lett.* **2010**, *96*, 183502.

[16] Y. Ko, M. Kwon, W. K. Bae, B. Lee, S. W. Lee, J. Cho, *Nat. Commun.* **2017**, *8*, 536.

[17] X. Wang, A. Sumboja, W. L. Foo, C. Y. Yan, K. Tsukagoshi, P. S. Lee, *RSC Adv.* **2013**, *3*, 15827–15833.

[18] N. Liu, Y. Gao, *Small* **2017**, *13*, 1701989.

[19] L. Liu, Z. Niu, L. Zhang, W. Zhou, X. Chen, S. Xie, *Adv. Mater.* **2014**, *26*, 4855–4862.

[20] R. Brooke, J. Åhlin, K. Hübscher, O. Hagel, J. Strandberg, A. Sawatdee, J. Edberg, *J. Energy Storage* **2022**, *50*, 104191.

[21] I. Nam, G.-P. Kim, S. Park, J. W. Han, J. Yi, *Energy Environ. Sci.* **2014**, *7*, 1095–1102.

[22] I. H. Oh, S. M. Lee, Y. W. Kim, S. Choi, I. Nam, S. T. Chang, *J. Mater. Chem. A* **2021**, *9*, 27672–27683.

[23] D.-B. Grys, B. Nijs, A. R. Salmon, J. Huang, W. Wang, W.-H Chen, O. A. Scherman, J. J. Baumberg, *ACS Nano* **2020**, *14*, 8689–8696.

[24] C.-M. Wang, C.-Y. Chen, W.-S. Liao, *Anal. Chim. Acta* **2021**, *1144*, 158–177.

[25] E. W. Washburn, *Phys. Rev.* **1921**, *17*, 273.

[26] S. Modha, C. Castro, H. Tsutsui, *Biosens. Bioelectron.* **2021**, *178*, 113026.

[27] C. Renault, J. Koehne, A. J. Ricco, R. M. Crooks, *Langmuir* **2014**, *30*, 7030–7036.

[28] S. M. Lee, I. H. Oh, I. Nam, S. T. Chang, *Int. J. Energy Res.* **2021**, *45*, 15438–15451.

[29] G. Geng, P. Chen, G. Guan, Y. Liu, C. Yang, N. wang, M. Liu, *RSC Adv.* **2017**, *7*, 51838.

[30] B. Ballarin, M. C. Cassani, D. Tonelli, E. Boanini, S. Albonetti, M. Blosi, M. Gazzano, *J. Phys. Chem. C* **2010**, *114*, 9693–9701.

[31] T.-H. Lin, C.-W. Lin, H.-H. Liu, J.-T. Sheu, W.-H. Hung, *Chem. Commun.* **2011**, *47*, 2044–2046.

[32] X. Huang, Y. Li, Y. Chen, E. Zhou, Y. Xu, H. Zhou, X. Duan, Y. Huang, *Angew. Chem.* **2013**, *125*, 2580–2584; *Angew. Chem. Int. Ed.* **2013**, *52*, 2520–2524.

[33] L. Mao, K. Zhang, H. S. O. Chan, J. Wu, *J. Mater. Chem.* **2012**, *22*, 1845–1851.

[34] Z. Ren, J. Li, J. Ren, S. Wang, Y. Qiu, J. Yu, *Sci. Rep.* **2016**, *6*, 20021.

[35] X. Dai, M. Zhang, J. Li, D. Yang, *RSC Adv.* **2020**, *10*, 15860–15869.

[36] M. Yuan, F. Luo, Y. Rao, J. Yu, Z. Wang, H. Li, X. Chen, *Carbon* **2021**, *183*, 128–137.

[37] H. Zhao, G. Han, Y. Chang, M. Li, Y. Li, *Electrochim. Acta* **2013**, *91*, 50–57.

[38] M. Zhang, D. Yang, J. Li, *Appl. Surf. Sci.* **2021**, *541*, 148546.

[39] M. Li, J. Yu, X. Wang, Z. Yang, *Appl. Surf. Sci.* **2020**, *530*, 147230.

[40] L. Zhang, P. Zhu, F. Zhou, W. Zeng, H. Su, G. Li, J. Gao, R. Sun, C. Wong, *ACS Nano* **2016**, *10*, 1273–1282.

[41] Y. He, W. Chen, X. Li, Z. Zhang, J. Fu, C. Zhao, E. Xie, *ACS Nano* **2013**, *7*, 174–182.

[42] Z. Peng, J. Lin, R. Ye, E. L. G. Samuel, J. M. Tour, *ACS Appl. Mater. Interfaces.* **2015**, *7*, 3414–3419.

[43] Y. Wang, Y. Shi, C. X. Zhao, J. I. Wong, X. W. Sun, H. Y. Yang, *Nanotechnology* **2014**, *25*, 094010.

[44] W. Liu, C. Lu, H. Li, R. Y. Tay, L. Sun, X. Wang, W. L. Chow, X. Wang, B. K. Tay, Z. Chen, J. Yan, K. Feng, G. Lui, R. Tjandra, L. Rasenthram, G. Chiu, A. Yu, *J. Mater. Chem. A* **2016**, *4*, 3754.

[45] H. Xiao, Z.-S. Wu, F. Zhou, S. Zheng, D. Sui, Y. Chen, X. Bao, *Energy Storage Mater.* **2018**, *13*, 233–240.

[46] J. Qin, S. Wang, F. Zhou, P. Das, S. Zheng, C. Sun, Z. Bao, Z.-S. Wu, *Energy Storage Mater.* **2019**, *18*, 397–404.

[47] C. J. Zhang, M. P. Kremer, A. S. -Ascaso, S.-H. Park, N. McEvoy, B. Anasori, Y. Gogotsi, V. Nicolosi, *Adv. Funct. Mater.* **2018**, *28*, 1705506.

[48] J. Wang, V. K. Bandari, D. Karnaushenko, Y. Li, F. Li, P. Zhang, S. Baunack, D. D. Karnaushenko, C. Backer, M. Faghih, T. Kang, S. Duan, M. Zhu, X. Zhuang, F. Zhu, X. Feng, O. G. Schmidt, *ACS Nano* **2019**, *13*, 8067–8075.

[49] F. Xia, S. Xu, Q. Gao, X. Wang, *in: 2020 IEEE 33rd International Conference on Micro Electro Mechanical Systems (MEMS)*, **2020**, 614–617.

[50] H. Chen, Z. Mao, S. Chen, Y. Zhang, X. Hu, S. Xin, Y. Bai, *ACS Appl. Energ. Mater.* **2021**, *4*, 10948–10957.

[51] Z. Ma, J. Zhao, Y. Fan, X. Qin, G. Shao, *J. Alloys Compd.* **2022**, *920*, 166012.